arXiv:1609.07351v2 [quant-ph] 26 Sep 2016

Second-order decoherence mechanisms of a transmon qubit probed with thermal microwave states

J. Goetz,[1,2,*] F. Deppe,[1,2] P. Eder,[1,2,3] M. Fischer,[1,2,3] M. Müting,[1,2] J. P. Martínez,[4,5] S. Pogorzalek,[1,2] F. Wulschner,[1,2] E. Xie,[1,2,3] K. G. Fedorov,[1,2] A. Marx,[1] and R. Gross[1,2,3,†]

[1] *Walther-Meißner-Institut, Bayerische Akademie der Wissenschaften, 85748 Garching, Germany*
[2] *Physik-Department, Technische Universität München, 85748 Garching, Germany*
[3] *Nanosystems Initiative Munich (NIM), Schellingstraße 4, 80799 München, Germany*
[4] *Universite Grenoble Alpes, Institut NEEL, F-38000 Grenoble, France*
[5] *CNRS, Institut NEEL, F-38000 Grenoble, France*

(Dated: prel. version September 27, 2016)

Thermal microwave states are omnipresent noise sources in superconducting quantum circuits covering all relevant frequency regimes. We use them as a probe to identify three second-order decoherence mechanisms of a superconducting transmon. First, we quantify the efficiency of a resonator filter in the dispersive Jaynes-Cummings regime and find evidence for parasitic loss channels. Second, we probe second-order noise in the low-frequency regime and demonstrate the expected T^3 temperature dependence of the qubit dephasing rate. Finally, we show that qubit parameter fluctuations due to two-level states are enhanced under the influence of thermal microwave states. In particular, we experimentally confirm the T^2-dependence of the fluctuation spectrum expected for noninteracting two-level states.

I. INTRODUCTION

Solid-state based quantum circuits are attractive for quantum information systems due to their design flexibility and the possibility to engineer and tune interactions. This is particularly true for superconducting quantum circuits which are widely used for quantum computing [1] and quantum simulation [2], or the generation of quantum entanglement [3]. One advantage of superconducting circuits is that they provide strong [4, 5] or even ultrastrong [6–8] and well controllable [9–13] interaction. However, while strong interaction enables simple and fast manipulation of quantum circuits, it also goes along with strong coupling to environmental fluctuations (noise), thereby limiting the coherence properties. For superconducting quantum circuits, the impact of environmental noise has been widely studied both in theory and experiment. In particular, noise sources that couple coherently to qubits [14–16], as well as Markovian [17–21], or non-Markovian ($1/f$) noise sources [22–27] have been analyzed. To optimize the coherence properties, several strategies to decouple a qubit from the environmental noise have been developed. In the first place, the most convenient way to suppress noise over a broad frequency range is to place the qubit inside a superconducting resonator [28]. This concept is efficient, when the qubit transition frequency is far detuned from the resonator frequency by an amount δ much larger than their coupling strength g. Nevertheless, even in this case, noise still couples to the qubit in second-order with strength g^2/δ. In the second place, fluctuations that modify the qubit transition frequency ω_q can be noticeably suppressed by tuning the qubit to an operation point where the derivative of ω_q with respect to the fluctuating quantity vanishes [23, 25, 27, 29, 30]. Again, even at such a sweet spot, second-order coupling of environmental fluctuations can be a source for decoherence [31–33]. In addition to these decoherence processes, intrinsic qubit parameters such as its relaxation rate can be fluctuating in time [34–37]. One prominent source for these fluctuations are two-level states (TLSs) mediating low-frequency noise to the qubit.

The three second-order decoherence mechanisms mentioned above can be reliably studied with propagating thermal fields because their power spectral density $\mathcal{S}(\omega)$ can be adjusted with a high accuracy by controlling the temperature of a black-body radiator [38–40]. Furthermore, $\mathcal{S}(\omega)$ is white for low frequencies and sufficiently smooth at the qubit transition frequency, which allows for a quantitative analysis of second-order decoherence mechanisms. Besides the fact that thermal fields are an accurate control knob to study second-order effects of noise, their omnipresence in superconducting circuits [41–47] naturally results in a strong demand to investigate their second-order influence on the coherence properties of superconducting quantum circuits.

In this work, we systematically study the effect of the second-order coupling between thermal fields generated by a black-body radiator and a superconducting transmon qubit [30] placed in a superconducting resonator. We analyze the three individual decoherence mechanisms depicted in Fig. 1 (a). The novel aspect of our experiments is that we can either irradiate the qubit directly or via the resonator filter function with thermal noise of controllable power spectral density while keeping the qubit at the base temperature of a dilution refrigerator. This allows us to quantify the impact of thermal noise without suffering from parasitic effects such as quasiparticle generation in the superconducting circuits. After discussing the experimental setup in Sec. II, we analyze the first de-

* jan.goetz@wmi.badw.de
† rudolf.gross@wmi.badw.de

coherence mechanism, which is relaxation of the qubit due to dispersively coupled thermal noise (see Sec. III). In the dispersive Jaynes-Cummings regime, noise at the resonator frequency couples in second-order. In our experiments, we find a coupling to broadband fields, which is enhanced as compared to that expected from the Purcell filter effect of the resonator. Furthermore, using coherent states and narrowband shot noise, we demonstrate the counter-intuitive effect that the qubit relaxation rate is decreasing for increasing field strengths. In Sec. IV, we discuss the situation when the thermal noise field is directly irradiated on the qubit via a near-field antenna without the cavity filter. At the flux sweet spot, this direct irradiation reveals the influence of second-order-coupled noise on the qubit dephasing rate. In particular, we observe the expected [31, 33] T^3 temperature dependence of the qubit dephasing rate. Finally, in Sec. V, we show that low-frequency fluctuations of the qubit relaxation rate are related to the temperature of the black-body radiator if the field is not Purcell filtered. We can explain this effect by the presence of two-level fluctuators in the spatial vicinity of the qubit, which change the effective noise spectral density.

Our work establishes thermal fields as an important tool to probe the coherence properties of superconducting quantum circuits. In this way, we gain important insight into second-order decoherence mechanisms of superconducting qubits. Furthermore, our quantitative analysis of the decoherence rates is crucial to optimize the performance of superconducting qubits, which is necessary for many quantum computation and communication protocols.

II. EXPERIMENTAL TECHNIQUES

The experimental setup to study the effect of thermal noise on a superconducting transmon qubit is sketched in Fig. 1 (a). In two different cooldowns, we couple a thermal noise source either directly through a near-field antenna or indirectly via a superconducting resonator to a transmon qubit. In our experiments, we measure the qubit coherence properties as a function of the power spectral density of the noise source, which defines the average number of thermal photons. We generate the propagating thermal fields at low temperatures using a 50 Ω-matched 30 dB attenuator. The attenuator is thermally decoupled from the sample box and only weakly coupled to the base temperature stage of a dilution refrigerator. The qubit is located inside a sample box, which is mounted to the base temperature stage and stabilized to $T_\mathrm{i} = 35\,\mathrm{mK}$ (see App. A for details). Heating the attenuator up to 1.5 K results in the emission of black-body radiation with a power spectral density controlled by the attenuator temperature. The average number of emitted thermal noise photons $n_\mathrm{th}(\omega, T) = [\exp(\hbar\omega/k_\mathrm{B}T) - 1)]^{-1}$ at frequency ω is given by the Bose-Einstein distribution [48] of a black-body radiator. The power spectral density of the propagating thermal fields emitted by a 50 Ω-matched attenuator into a 50 Ω-matched line reads [38]

$$\mathcal{S}(\omega, T) = \hbar\omega(n_\mathrm{th} + 1/2) = \frac{1}{2}\hbar\omega \coth\left(\frac{\hbar\omega}{2k_\mathrm{B}T}\right). \quad (1)$$

A physical understanding of this expression is obtained by writing the units as W/Hz. In this way, one immediately sees that $\mathcal{S}(\omega, T)$ describes the noise power per Hz of bandwidth. In Eq. (1), $\mathcal{S}(\omega, T)$ is reduced by a factor of four compared to the well-known [49, 50] Johnson-Nyquist noise $4k_\mathrm{B}T$ because we model the attenuator as a 50 Ω-matched noise source [38, 51]. We probe indirectly coupled thermal fields by operating the qubit in the dispersive regime [case (i) in Fig. 1 (a)], where the detuning $\delta \equiv \omega_{\mathrm{q},0} - \omega_\mathrm{r}$ fulfills $g/\delta \ll 1$. Here, $g/2\pi \simeq 67\,\mathrm{MHz}$ is the qubit-resonator coupling strength,

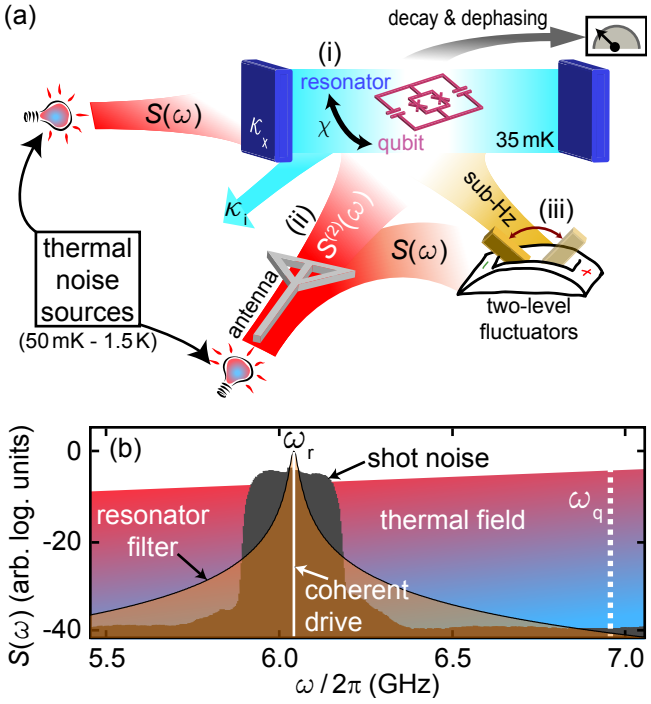

Figure 1. (a) Sketch of the experimental idea. We characterize the second-order coupling between a thermal noise source (black-body radiator of variable temperature) and a superconducting qubit by measuring the qubit decay and dephasing rate. The second-order coupling to the thermal noise field becomes relevant in the following situations: (i) When the qubit is dispersively coupled to a resonator acting as a filter for the noise field with spectral density $\mathcal{S}(\omega)$. (ii) When the qubit is directly irradiated by a noise field using a near-field antenna, but operated at a sweet spot making the second-order spectral density $\mathcal{S}^{(2)}(\omega)$ the leading contribution. (iii) When one or multiple two-level fluctuators change the noise spectral density in the sub-Hz regime. (b) Power spectral density of thermal fields, coherent states, and shot noise plotted versus frequency. All fields can be filtered by the Lorentzian filter function of a resonator. The dashed line shows the transition frequency of the qubit.

$\omega_r/2\pi \simeq 6.07\,\mathrm{GHz}$ is the resonator frequency, and $\omega_{q,0}/2\pi \simeq 6.92\,\mathrm{GHz}$ is the qubit transition frequency at the flux sweet spot. For a transmon qubit, which is not a perfect two-level system, the dispersive shift [30] $\chi \equiv -g^2 E_C/(\delta^2 - \delta E_C) \simeq -2\pi \times 3.11\,\mathrm{MHz}$ depends on the transmon charging energy $E_C \simeq h \times 315\,\mathrm{MHz}$. To probe dispersively coupled noise, we send the thermal fields through the coupling capacitor of the resonator. To analyze second-order contributions of thermal fields [case (ii) in Fig. 1 (a)], we use the on-chip antenna to directly irradiate the qubit with the thermal noise field without any cavity filtering. Since the antenna represents a short circuit of a 50 Ω line, the thermal noise field generates a thermal noise current, coupling thermal flux noise to the SQUID loop of the transmon qubit. Note that at the flux sweet spot, the second-order power spectral density [31, 33] (units to be read as W^2/Hz)

$$\mathcal{S}^{(2)}(\omega) = \omega \left[\frac{\hbar^2\omega^2 + 4\pi^2 k_B^2 T^2}{12\pi}\right] \coth\left(\frac{\hbar\omega}{2k_B T}\right) \qquad (2)$$

of thermal fields is relevant because first-order fluctuations are strongly suppressed at the sweet spot. The second-order power spectral density, however, still couples intensity fluctuations to the qubit. Finally, we probe the influence of thermal fields on the low-frequency fluctuations of qubit parameters [case (iii) in Fig. 1 (a)] by repeatedly measuring the qubit relaxation rate on a timescale of three hours such that the lowest detectable switching frequency of the fluctuators is approximately 0.1 mHz. We perform these measurements for dispersively coupled noise and for noise, which couples directly through the antenna.

We calibrate the thermal noise power on the input lines using the qubit as a power detector for the mean photon number n_r in the resonator. Since we generate the thermal states outside the resonator, the resonator population is calculated as a cavity field that is coupled to three bosonic baths defined in the following by the subscript $j \in \{i, x, a\}$. The first bath is the direct sample environment with a thermal occupation number n_i coupling via the internal loss rate $\kappa_i/2\pi \simeq 50\,\mathrm{kHz}$ to the resonator. Second, the resonator is coupled with strength $\kappa_x/2\pi \simeq 8.5\,\mathrm{MHz}$ to modes on the readout line, which can be thermally occupied by heating the attenuator, thereby generating the occupation number n_x. Third, there is the coupling via $\kappa_{a,r}$ to the antenna line photons n_a. These can also be controlled by a heatable attenuator. The additional subscript r denotes the antenna coupling to the resonator while the antenna coupling to the qubit is defined as $\kappa_{a,q}$. We provide a detailed discussion about the broadband coupling of thermal fields in App. B, where we show that it results in the resonator population $n_r(\omega, T) \approx \mathcal{F}_L(\omega) \sum_j \kappa_j n_{th,j}(\omega, T)$. In this expression, $\mathcal{F}_L(\omega) = (\kappa_{tot}/2)/[(\kappa_{tot}/2)^2 + (\omega - \omega_r)^2]$ is the Lorentzian filter function of the resonator shown in Fig. 1 (b) and $\kappa_{tot} \equiv \sum_j = \kappa_i + \kappa_x + \kappa_{a,r}$ is the total loss rate of the resonator. Because of the low sample temperature of 35 mK, we can neglect thermal photons coupling via κ_i. Then, on resonance, the steady state limit of the Markovian master equation [Eq. (B2)] describing the resonator yields $n_r(\omega_r, T_x, T_a) = [\alpha_x \kappa_x n_x(\omega_r, T_x) + \alpha_a \kappa_{a,r} n_a(\omega_r, T_a)]/\kappa_{tot}$. Here, the factors α_x and α_a account for losses in the microwave lines between attenuator and sample. Because we use the very same combination of attenuator and coaxial cables for the two cool-downs, we assume $\alpha_x = \alpha_a \equiv \alpha$ in the following. In the dispersive regime, we calibrate this factor by measuring the ac-Stark shift [52] of the qubit

$$\delta\omega_{q,x}(T_x) = 2\chi\alpha\kappa_x\, n_x(T_x)/\kappa_{tot} + \delta\omega_{q,a}(50\,\mathrm{mK})\,, \qquad (3)$$
$$\delta\omega_{q,a}(T_a) = 2\chi\alpha\kappa_{a,r} n_a(T_a)/\kappa_{tot} + \delta\omega_{q,x}(50\,\mathrm{mK})\,. \qquad (4)$$

From sweeping the temperature T_x of the feedline attenuator, we obtain $\alpha \simeq 4.1\,\mathrm{dB}$ using a numerical fit of Eq. (3) as shown in Fig. 2. From sweeping the antenna line attenuator, we extract the negligibly small coupling rate $\kappa_{a,r}/2\pi \simeq 30\,\mathrm{kHz}$. We note that we also use coherent states and shot noise with the spectral density shown in Fig. 1 (b) in our experiments. These fields are generated at room temperature with state-of-the-art microwave equipment as discussed in App. A. We calibrate the photon number of these fields with ac-Stark shift measurements similar to the ones discussed above.

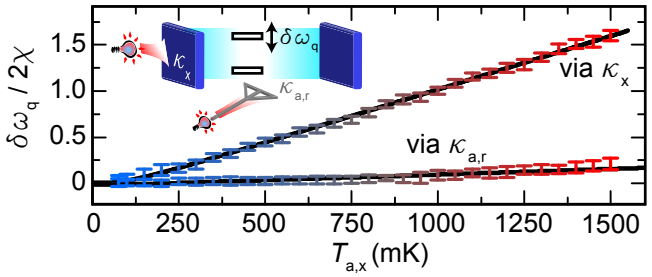

Figure 2. ac-Stark shift of the qubit transition frequency plotted versus temperature of the heatable attenuator in the readout line (via κ_x) or the antenna line (via $\kappa_{a,r}$). Solid lines are fits using Eq. (3) and Eq. (4) while the inset depicts the experimental configuration.

In the absence of external microwave fields and at the flux sweet spot, the qubit is relaxation-limited with average coherence times of approximately 500 ns. In particular, we find typical values of the Ramsey decay rate $\gamma_{2,R}/2\pi \simeq 2.1\,\mathrm{MHz}$, the spin-echo decay rate $\gamma_{2,se}/2\pi \simeq 1.9\,\mathrm{MHz}$, and the energy decay (relaxation) rate $\gamma_1/2\pi \simeq 3.9\,\mathrm{MHz}$ [cf. Fig. 3 (a) – (c)]. This relaxation rate is a factor of ten larger than the expected Purcell rate and most likely dominated by loss into the Si/SiO_2 substrate and into the on-chip antenna. The above numbers imply a pure dephasing rate $\gamma_\varphi = \gamma_{2,R} - \gamma_1/2 \simeq 2\pi \times 150\,\mathrm{kHz}$. In general, we find that the irradiation of thermal states onto the qubit increases the decoherence rates, which is discussed in detail in Sec. III – Sec. V.

We measure the coupling $\kappa_{a,q}$ between antenna and

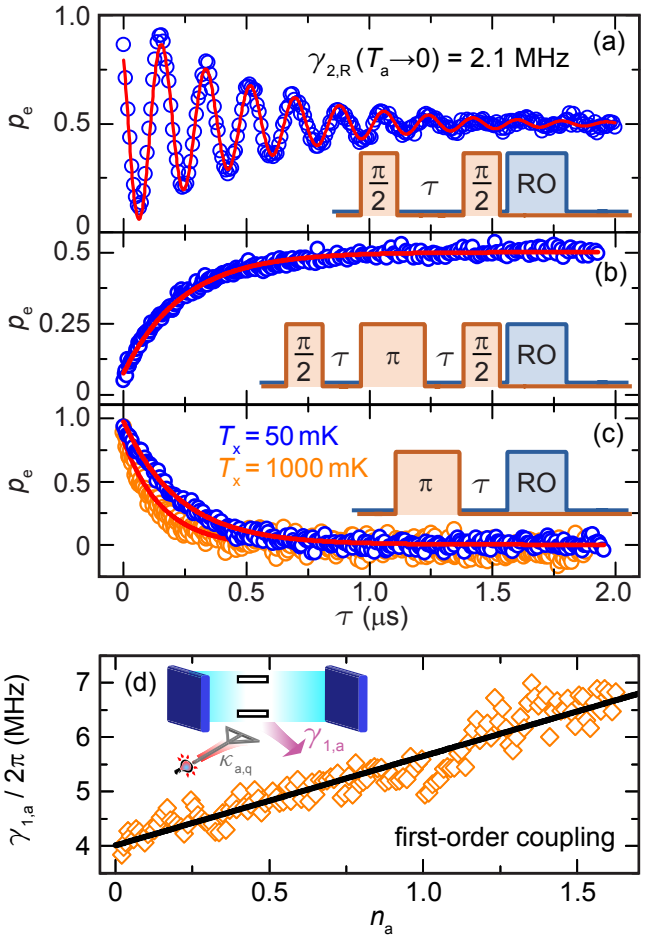

Figure 3. (a) Probability p_e to find the qubit in the excited state as a function of the free evolution time for the Ramsey pulse sequence (inset). Red envelopes indicate qubit control pulses, blue envelopes the readout pulse to the resonator. The solid lines are fits to the data points (circles). (b) As in panel (a), but for the spin-echo sequence. (c) As in panel (a), but for the relaxation sequence. T_x indicates the temperature of the readout line attenuator. (d) Qubit relaxation rate plotted versus the number of thermal photons emitted from the antenna line attenuator. The solid line is a linear fit and the inset depicts a sketch of the experimental setup.

qubit by irradiating the qubit with thermal noise (first-order coupling) through the antenna line. Thermal noise is Gaussian and weak [$\mathcal{S}(\omega) \ll \hbar\omega$] for average photon numbers $n_a \approx 1$. Hence, we can apply the spin-boson model and Fermi's golden rule to obtain $\gamma_1 = \mathcal{S}(\omega_q)/2\hbar$. This relation has been widely used to measure the frequency dependence $\mathcal{S}(\omega)$ of different noise sources by tuning the qubit transition frequency [17–21, 27, 28, 53]. Here, we use a complementary approach and vary the magnitude of $\mathcal{S}(\omega_q = \text{const.})$ in a controlled way by varying the temperature of the black-body radiator (antenna line attenuator). The resulting qubit decay rate

$$\gamma_{1,a}(T_a) = \gamma_1 + \kappa_{a,q} n_a(\omega_q, T_a)/2 \equiv \gamma_1 + \delta\gamma_{1,a}(T_a)\,, \quad (5)$$

is enhanced by $\delta\gamma_{1,a}$ compared to the intrinsic decay rate γ_1. We expect $\gamma_{1,a}$ to increase linearly with $\mathcal{S}(\omega_q)$ which is proportional to the average photon number n_a generated in the resonator by the thermal noise applied by the antenna. This is in very good agreement with the experimental data shown in Fig. 3 (d). From a linear fit of Eq. (5) to the data, we obtain the antenna qubit coupling rate $\kappa_{a,q} = 820$ kHz, which means that approximately 1/5 of the total qubit relaxation can be attributed to decay into the antenna. The accuracy of the qubit acting as noise spectrometer is limited by the standard deviation $\sigma/2\pi \simeq 215$ kHz of the data obtained from the fit. This scatter can be attributed to additional low-frequency fluctuations of the relaxation rate discussed in detail in Sec. V. We want to emphasize that changing the temperature of the thermal noise source has no effect on quasiparticle loss [54, 55] since the sample itself is kept at a constant temperature. Furthermore, radiation that directly generates quasiparticles, i.e., radiation with the gap frequency $\Delta_0/h \simeq 80$ GHz of Al is strongly suppressed in the coaxial cables.

III. THERMAL FIELDS IN THE DISPERSIVE JAYNES-CUMMINGS REGIME

In contrast to the direct irradiation of the qubit by thermal noise as discussed above, in this section we study the effect of thermal noise, which we apply to the transmon qubit through a superconducting resonator. Then, the resonator acts as a narrow filter for the broadband thermal noise. Since the qubit is far detuned from the resonator frequency ($|\chi| \ll g$), noise couples only in second-order to the qubit, which can be described within the dispersive limit of the Jaynes-Cummings model. There, the power spectral density $\mathcal{S}(\omega_q)$ at the qubit frequency is strongly reduced due to the Lorentzian filter function of the resonator. Hence, we obtain the reduced vacuum Purcell decay rate [56, 57] $\gamma_P \equiv \kappa_x |\chi/\delta| \simeq 2\pi \times 30$ kHz. Nevertheless, also the thermal noise spectral density $\mathcal{S}(\omega_r)$ at the resonator frequency couples dispersively to the qubit with the coupling rate χ in second-order approximation [58]. In an elaborate treatment, the broadband nature of thermal fields requires an exact transformation of the dispersive Jaynes-Cummings Hamiltonian, which takes sideband decay into account [59]. This transformation yields the total relaxation rate in the dispersive regime

$$\gamma_1^d = \gamma_1 \left[1 - \frac{|\chi|}{\delta}[2n_r + 1]\right] + \gamma_P[2n_q + 1] + 4\frac{|\chi|}{\delta}\frac{\mathcal{S}(\delta)}{\hbar} \times [2n_r + 1]\,, \quad (6)$$

where the effective photon number at the qubit frequency is defined as $n_q \equiv \alpha n_{th}(\omega_q, T_x)$. The first term in Eq. (6) is the main contribution to the total relaxation rate γ_1^d. The second term describes the Purcell decay rate due to the noise power $\mathcal{S}(\omega_q)$ at the qubit frequency. The last term accounts for a sideband decay resulting from the

combined action of resonator photons at ω_r and thermal noise photons at $\delta \equiv \omega_q - \omega_r \simeq 850\,\mathrm{MHz}$ as shown in Fig. 4 (a). Interestingly, a reduction of the decay rate can be obtained with increasing resonator photon number n_r if $\gamma_1 > 4\mathcal{S}(\delta)/\hbar$ due to the mixing of qubit and resonator states [59]. We calibrate the strength of the spectral density $\mathcal{S}(\delta)$ by selectively driving at the resonator frequency, which changes n_r while leaving n_q and $\mathcal{S}(\delta)$ in Eq. (6) constant. To this end, we use a coherent drive at the resonator frequency, and measure the change of the relaxation rate

$$\delta\gamma_{1,r}(n_r) = 2n_r \frac{|\chi|}{\delta}\left[\frac{4\mathcal{S}(\delta)}{\hbar} - \gamma_1\right], \qquad (7)$$

which is obtained by keeping only the n_r-dependent terms on the right hand side of Eq. (6). Equation (7) directly shows that for $4\mathcal{S}(\delta)/\hbar < \gamma_1$, we can reduce the qubit relaxation rate. As shown in Fig. 4 (b), we observe this decrease of the qubit relaxation rate for a coherent state that changes the resonator population in a controlled way. Using a numerical fit based on Eq. (7), we find a spectral density $\mathcal{S}(\delta) \simeq 1.32 \times 10^{-28}\,\mathrm{W/Hz}$. We obtain the same result when irradiating the resonator with shot noise that has a spectral density as shown in Fig. 1 (b). We note that the overall qubit decoherence rate given by $\gamma_2 = \gamma_\varphi + \gamma_1/2$ is nevertheless increasing due to the additional dephasing from noise in the photon number as discussed in detail in Ref. 60.

When we apply broadband thermal fields through the resonator input, we experimentally verify the three competing mechanisms present in Eq. (7). First, the increasing noise power spectral density $\mathcal{S}(\omega_r)$ at the resonator frequency is reducing qubit relaxation due to the mixing of qubit and resonator states as discussed already above. Second, the increasing noise power spectral density at the qubit transition frequency attenuated by the Purcell filtering of the resonator, $\mathcal{S}(\omega_q)\mathcal{F}_L(\omega_q)$, causes additional relaxation. Third, the increasing noise power spectral density at the detuning frequency δ attenuated by the Purcell filtering effect, $\mathcal{S}(\delta)\mathcal{F}_L(\delta)$, causes additional relaxation. This mechanism can be viewed as a sideband decay. Hence, the overall relaxation rate increases with increasing number of thermal photons stored inside the resonator as shown in Fig. 4 (b). When comparing the measured total relaxation rate γ_1^d with a calculation according to Eq. (6) [dotted line in Fig. 4 (b)], we find that the measured decay rate is significantly larger than expected. Hence, we fit Eq. (6) to the data and use $n_q(T_x)$ as a free parameter [dashed line in Fig. 4 (b)]. We find that the coupling of the thermal noise fields to the qubit is enhanced by a factor of 10. Because the qubit is galvanically decoupled from the resonator and the sample is stabilized at 35 mK, this additional coupling is most likely mediated by parasitic modes of the sample box [28, 61]. Among others, such modes can be slotline, parallel plane, and surface wave modes with resonance frequencies close to the qubit transition frequency. Our results show that this mechanism originating from the broadband nature

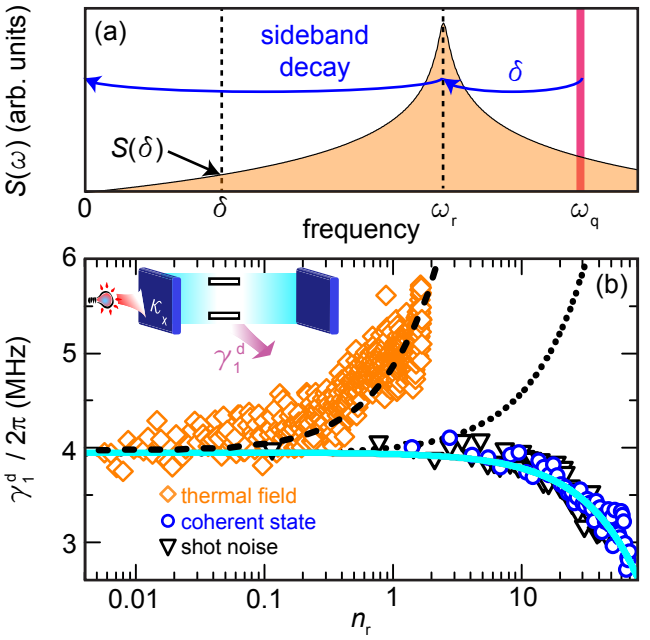

Figure 4. (a) Schematic drawing of sideband decay due to a finite noise power spectral density $\mathcal{S}(\delta)$ at the detuning frequency $\delta = \omega_q - \omega_r$. (b) Qubit relaxation rate for microwave fields coupling the qubit through the resonator (see inset for setup sketch) plotted versus the average photon number n_r. The solid line is a numerical fit using Eq. (7). The dotted line is a calculation based on Eq. (6) modeling the expected increase due to thermal fields. For the dashed line we use a numerical fit of Eq. (6), where the enhanced relaxation rate is modeled by $n_q(T_x)$ as a free parameter.

of the noise fields can dominate over the associated Purcell rate originating from the finite bandwidth of the resonator. Therefore, great care must be taken in the microwave design of sample holders and chip layout in order to minimize losses from broadband fields.

IV. SECOND-ORDER FLUX NOISE FROM THERMAL FIELDS

In addition to the relaxation processes discussed above, the qubit can suffer from dephasing due to propagating thermal fields, even if the resonator filters them. The main contribution in this context is noise, which introduces dephasing by modulating the qubit frequency via the ac-Stark shift [41, 44, 52]. We analyze this effect for thermal fields on the readout line in detail in Ref. 60. Here, we focus on dephasing caused by second-order intensity fluctuations of the thermal fields emitted from the heatable attenuator in the antenna line. The thermal noise fields manifest as current fluctuations on the short-circuited on-chip antenna, which couple magnetic flux noise into the SQUID loop of the transmon qubit. Far away from the flux sweet spot, the qubit dephasing is dominated by the first-order noise power spectral

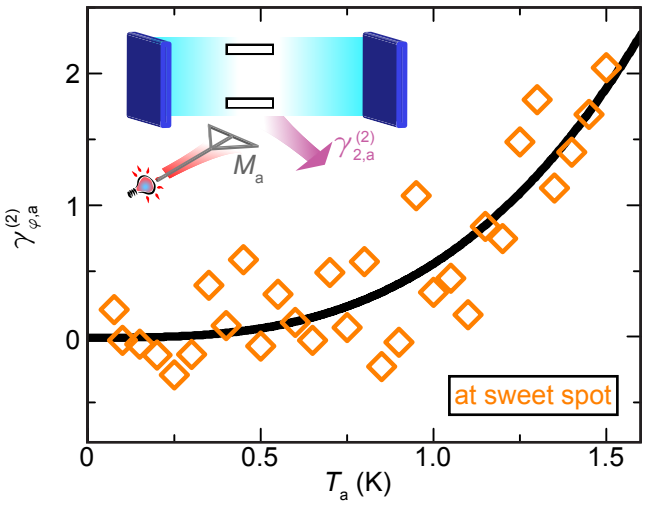

Figure 5. Thermally induced qubit dephasing rate $\gamma^{(2)}_{\varphi,\mathrm{a}}(T_\mathrm{a})$ measured as a function of the temperature T_a of the blackbody radiator as depicted in the inset. To isolate second-order effects, we operate the qubit at the flux sweet spot of the transmon qubit. The solid line is a numerical fit using Eq. (8).

density $\mathcal{S}(\omega\mapsto 0)$ defined in Eq. (1) due to the finite first-order transfer function (see App. C for details). At the flux sweet spot, however, the first-order transfer function vanishes while second-order fluctuations can still introduce dephasing. These fluctuations are characterized by the second-order power spectral density $\mathcal{S}^{(2)}(\omega)$ defined in Eq. (2). Using the second-order transfer function $\mathcal{D}^{(2)}_{\lambda,\mathrm{z}}=\pi^2\omega_{\mathrm{q},0}/2$ at the sweet spot, we find the thermally induced qubit dephasing rate [cf. Eq. (C10)]

$$\gamma^{(2)}_{\varphi,\mathrm{a}}(T_\mathrm{a}) = 2\pi\left[\frac{\pi^2}{4\sqrt{3}}\frac{M_\mathrm{a}^2}{L_\ell Z_0}\right]^2\left[\frac{k_\mathrm{B}T_\mathrm{a}}{\hbar}\right]^3, \qquad (8)$$

which follows a T_a^3 dependence. Here, M_a describes the mutual inductance between qubit and antenna, L_ℓ is the inductance of the SQUID loop, and Z_0 is the line impedance. In Fig. 5, we plot the qubit dephasing rate $\gamma^{(2)}_{\varphi,\mathrm{a}}(T_\mathrm{a})=\gamma_{2,\mathrm{R}}(T_\mathrm{a})-\gamma_{2,\mathrm{R}}(T_\mathrm{a}\mapsto 0)-\delta\gamma_{1,\mathrm{a}}(T_\mathrm{a})/2$ caused by the intensity fluctuations of the thermal noise field at the flux sweet spot of the transmon qubit. The temperature independent decay rate $\gamma_{2,\mathrm{R}}(T_\mathrm{a}\mapsto 0)$ and the thermally induced relaxation rate $\delta\gamma_{1,\mathrm{a}}(T_\mathrm{a})$ are discussed in Sec. II [see Fig. 3 (a) and Fig. 3 (d), respectively]. The additional dephasing rate follows the expected T_a^3 dependence with a scatter that is dominated by additional low-frequency fluctuations of the decay rate discussed in Sec. V. Fitting Eq. (8) to the data, we find a loop inductance $L_\ell\simeq 50\,\mathrm{pH}$ which is in reasonable agreement with the value of 100 pH estimated from the loop geometry. Here, we have used the mutual inductance $M_\mathrm{a}=1.3\,\mathrm{pH}$ obtained from measuring the induced flux shift of the qubit when applying a DC current through the antenna line. Our results show that second-order flux noise can induce residual dephasing in a transmon qubit, even if it is operated at the flux sweet spot. For typical temperatures ($T_\mathrm{a}<50\,\mathrm{mK}$) used in circuit QED experiments, however, we find that additional intensity fluctuations introduce only negligible dephasing of approximately 100 Hz because of the quadratic suppression $(k_\mathrm{B}T_\mathrm{a}/\hbar\omega_{\mathrm{q},0})^2$ [cf. Eq. (C10)]. Nevertheless, dephasing is not only determined by the relatively weak thermal contribution but also by stronger $1/f$ noise [23, 27]. Because $1/f$ noise also has a second-order contribution [33], our results show that this noise can be a possible source for the residual dephasing found for transmon qubits.

V. FLUCTUATING QUBIT PARAMETERS IN THE PRESENCE OF THERMAL FIELDS

In the following, we study the effect of thermal fields on the frequency spectrum of fluctuating qubit parameters. In particular, we analyze low-frequency variations of the relaxation rate of a transmon qubit. This phenomenon was also observed for flux qubits [35, 37], for transmon qubits in a 3D cavity and phase qubits [36], as well as for the resonance frequency of superconducting resonators [62]. One particular mechanism that can generate low-frequency fluctuations are TLSs [36, 63] in the spatial vicinity of the qubit. The fluctuation rate of the TLSs is influenced by the thermal field as depicted in Fig. 6.

Each individual TLS provides a Lorentzian shaped noise spectral density, which is centered around its excitation frequency $\omega_\mathrm{tls}=\sqrt{\varepsilon^2+\Delta^2}/\hbar$. Here, ε is the asymmetry energy and Δ is the tunnel splitting. Because the TLSs are coupled to each other via dipole or strain-mediated interaction [64], each TLS eigenfrequency depends on the state of the other TLSs. The low-frequency variations of the TLS configuration results in low-frequency fluctuations of the noise power spectral density $\mathcal{S}(\omega_\mathrm{q},t)$ generated by the TLSs. Consequently, the qubit relaxation rate $\gamma_1(t)=\mathcal{S}(\omega_\mathrm{q},t)/2\hbar$ starts fluctuating. Since qubit parameter fluctuations are typically recorded in the sub-Hz regime where $\hbar\omega\ll k_\mathrm{B}T$, we assume a white spectrum proportional to $k_\mathrm{B}T$ for the contribution of the environmental heat bath. For a distribution $P(\varepsilon,\Delta)d\varepsilon d\Delta\propto\varepsilon^x\Delta^{-1}d\varepsilon d\Delta$ of TLSs, we expect a T^{2+x}-dependence to be the dominant contribution to the

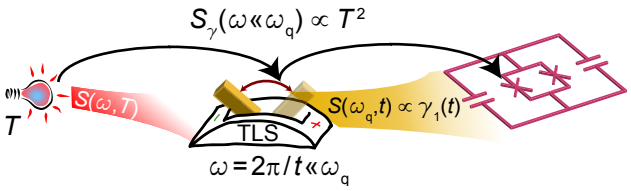

Figure 6. TLS-mediated relaxation rate fluctuations. The thermal field influences the TLS fluctuation rate causing fluctuations of the noise power spectral density $\mathcal{S}(\omega_\mathrm{q},t)$.

spectrum of γ_1 [36]. This contribution arises from those TLSs, which are detuned by $\delta\omega \equiv |\omega_q - \omega_{tls}| \gg \gamma_{2,R}$. The exponent $x \geq 0$ is nonzero only for a finite interaction between the TLSs [36].

We experimentally characterize the fluctuations of the noise power spectral density by measuring fluctuations of the qubit relaxation rate $\gamma_1(t)$. To this end, we perform systematic long-time measurements of the relaxation rate as a function of the temperatures T_x and of T_a ranging from 50 mK to 1500 mK. Each measurement is comprised of individual measurement traces taken at a repetition rate of 100 kHz, where the resonator is probed with 2 µs long traces with 250 MHz sampling rate. We average 4×10^5 of these measurements to extract the decay rate at a particular moment and then wait for 6 s such that individual data points are recorded at a rate of approximately 0.1 Hz. A typical series of relaxation measurements at $T_a = 1500$ mK over 200 min is shown in Fig. 7 (a). Here, we observe a standard deviation $\sigma/2\pi \simeq 320$ kHz from the mean relaxation rate $\langle\gamma_1\rangle/2\pi \simeq 6.25$ MHz. Even though the absolute value of σ seems large compared to other works [36], the relative scatter $\sigma/\langle\gamma_1\rangle \simeq 0.05$ is comparable. In our experiments, we observe no systematic influence of the temperature on σ for sweeps of T_a or T_x. To obtain more insight into the nature of the fluctuations, we investigate their spectral distribution. To this end, we calculate the Fourier transform $\mathcal{S}_\gamma(\omega) = \hbar/2\pi \int \mathrm{d}t\, \langle\gamma_1(t)\gamma_1(0)\rangle e^{-\imath\omega t}$ of the autocorrelation function $\langle\gamma_1(t)\gamma_1(0)\rangle$ as shown in Fig. 7 (b). For low frequencies, the data follows a $\omega^{-\beta}$-dependence, and crosses over into a frequency-independent tail for frequencies larger than a characteristic frequency $\omega_c \simeq 1$ mHz. As shown in Fig. 7 (c), we find that $\beta_a \simeq 0.91 \pm 0.24$ and $\beta_x \simeq 0.96 \pm 0.19$ are approximately constant for thermal fields applied through antenna or resonator, respectively. This result is an extension of recent findings presented in Ref. 35, where $1/f$ fluctuations were analyzed up to a maximum temperature of 200 mK.

Let us now turn to the white-noise contribution μ_a above the characteristic frequency ω_c exemplarily shown in Fig. 7 (c) and sytematically plotted as a function of the antenna line attenuator in Fig. 7 (d). We observe an increase of μ_a with the temperature T_a. From a numerical fit based on the function $\mu_a = \mu_{a0} + aT_a^{2+x}$, we find $\mu_{a0} = 0.81 \times 10^{-24}$ W/Hz, $a = 1.1 \times 10^{-25}$ W/(Hz K^2), and $x = -0.01 \pm 0.13$. Hence, our results support the model presented in Ref. 36 where a bath of TLSs acts as a source for the fluctuations in the qubit relaxation rate. In particular, the negligible value of $x \simeq 0$ indicates that the TLSs relevant for our experiments are noninteracting. In contrast to μ_a, the white noise level μ_x is approximately independent of the thermal field [see Fig. 7 (d)]. In this case, the resonator filters the thermal fields and protects the TLSs from the external noise. Hence, from this model, a small resonator bandwidth and well-filtered feedlines are necessary in order to suppress externally activated switching of two-level fluctuators.

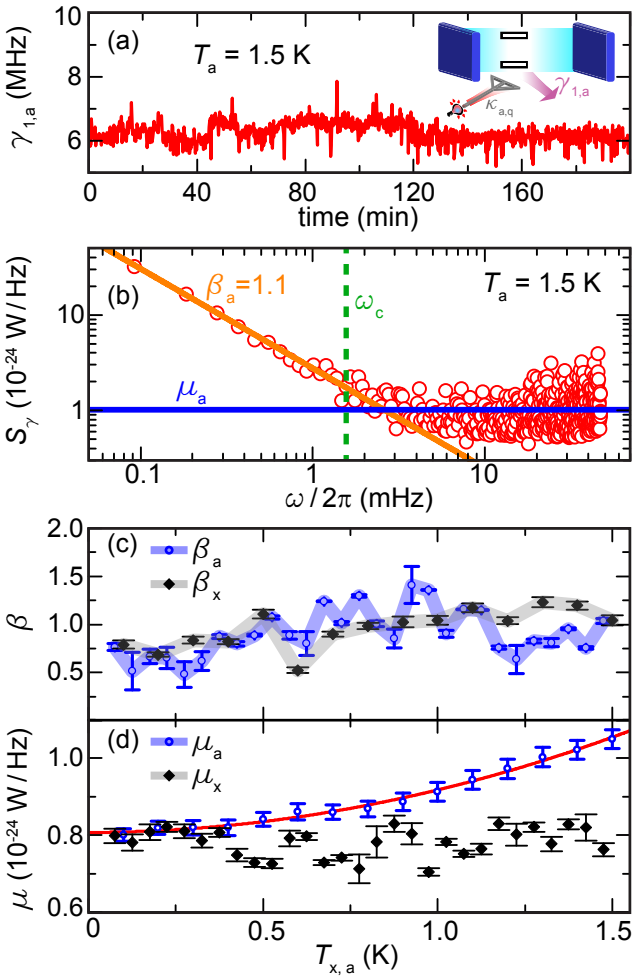

Figure 7. (a) Qubit relaxation rate recorded as a function of time recorded over a period of 200 min at $T_a = 1.5$ K. (b) Noise power spectral density for the data shown in panel (a). We obtain β from a fit to the data with frequencies below ω_c and μ as the mean value for points above ω_c. (c) Exponent β measured for $\omega < \omega_c$ versus temperature when applying thermal fields through the antenna or the resonator. Solid lines are guides to the eyes and error bars represent confidence intervals generated by the $\omega^{-\beta}$ fits. (d) Mean value μ of the white-noise contribution of thermal fields entering via the antenna or the resonator to $\mathcal{S}_\gamma$. The solid line is a fit as explained in text and error bars are the standard error of the mean.

VI. SUMMARY AND CONCLUSIONS

In summary, we have characterized the influence of propagating thermal microwaves onto second-order decoherence mechanisms of a transmon qubit in a resonator. Because we spatially and thermally separate the thermal emitter from the circuit QED sample, we are able to separate the influence of the thermal noise from the remaining loss channels of the qubit. This allows us to quantify three different second-order decoherence mechanisms. First, for the dispersive regime we find that the additional relaxation rate due to thermal fields applied

via the resonator is larger than expected from Purcell filtering. This is a strong hint to the relevance of additional coupling channels such as parasitic on-chip modes. Second, we observe the expected T^3 dependence for the additional dephasing due to second-order noise at the flux sweet spot. This finding may explain the residual dephasing rates found for superconducting qubits with long coherence times. Finally, we investigate the influence of thermal fields on the low-frequency spectrum of qubit parameter fluctuations. We find that thermal fields enhance the white contribution of the noise power spectral density if applied broadband via an on-chip antenna. Our data confirms a model of thermally activated TLSs interacting with the qubit. The resonator, however, can filter this effect efficiently.

ACKNOWLEDGEMENTS

We acknowledge financial support from the German Research Foundation through SFB 631 and FE 1564/1-1, EU projects CCQED, PROMISCE, the doctorate programs ExQM of the Elite Network of Bavaria, and the International Max Planck Research School "Quantum Science and Technology".

Appendix A: Sample and measurement details

We use a superconducting transmon qubit coupled to a quarter wavelength coplanar waveguide resonator as depicted in Fig. 8 (a). The qubit is characterized by the charging energy $E_C \simeq h \times 315\,\mathrm{MHz}$ and the total Josephson energy $E_{J0} \simeq h \times 20\,\mathrm{GHz}$ of the two SQUID junctions, which are used to tune the qubit transition frequency ($E_{J0}/E_C \simeq 64$). The qubit is made from a 110 nm thick Al/AlO_x/Al trilayer structure, shadow evaporated onto an undoped Si substrate. The silicon is covered with 50 nm thermal oxide on either side and has a resistivity larger than 1 kΩ cm at room temperature. We fabricate the 50 Ω-matched resonator with optical lithography from a 100 nm thick Nb film. We mount the sample chip onto a copper-plated printed circuit board inside a gold-plated sample box made from copper.

To generate thermal states on the readout and on the antenna line, we use heatable 30 dB attenuators integrated into the feedlines as depicted in Fig. 8 (b). For the coaxial cables connecting the attenuators to the sample box, we use 20 cm of Nb/CuNi UT47. The temperatures $T_{x,a}$ of the heatable attenuators used to vary the thermal photon number can be individually controlled between (0.050 ± 0.001) K and (1.50 ± 0.01) K. Thermal noise from higher temperature stages has only a negligible influence for our setup due to individual 10 dB attenuators in the feedlines at 4 K, 1.2 K, 0.75 K, and 0.3 K. To filter out noise entering the sample through the output-line in the frequency range between 4 GHz and 8 GHz, we use microwave circulators at 750 mK and at 35 mK. The circulators have an average leakage of 0.02 photons at 6 GHz due to their finite isolation. At the 4 K stage, we use a cryogenic high electron mobility transistor (HEMT) amplifier and further amplify the signal by a room temperature amplifier as shown in Fig. 8 (b). We implement a time-resolved, phase-sensitive measurement of the in-phase and quadrature components $I(t)$ and $Q(t)$ of the readout signal by heterodyne downconversion to an intermediate frequency $\omega_{if}/2\pi = 62.5\,\mathrm{MHz}$ and subsequent amplification. We digitize the signals using two analog-to-digital converters (ADC) with a sampling rate of 250 MHz and perform digital homodyning. In addition, we can read out the resonator via a vector network analyzer (VNA) for spectroscopic analysis of the sample. To generate pulsed sequences in the GHz regime, we mix a continuous microwave signal with a rectangular pulse generated by an arbitrary function generator (AFG). In addition to true thermal noise radiated from the attenuators, we can add noise generated by the AFG. By mixing this noise with a microwave signal, we upconvert the noise carrier frequency to the desired noise frequency ω_n. The AFG generates noise with a 500 MHz bandwidth, which has a quasi-Gaussian amplitude distribution. This noise has a constant variance of 1 V into 50 Ω, which we attenuate in a linear way when controlling the photon number. We additionally filter this noise before the upconversion to the carrier frequency ω_n by two 100 MHz low-pass filters. That way, the noise has a bandwidth of 200 MHz and an on/off ratio of 35 dB as shown in Fig. 1 (b).

From a two-tone experiment, we extract the qubit transition frequency [30] $\omega_q = \omega_{q,0}\sqrt{|\cos(\pi\Phi/\Phi_0)|}$ by fitting a Lorentzian function to the dip in the transmission spectrum shown in Fig. 9 (a). Here, Φ is the magnetic flux in the SQUID loop, which is generated by a superconducting coil outside the sample holder, and Φ_0 is the flux quantum. All experiments are carried out in the dispersive regime by keeping the average resonator population n_r below the critical photon number [65] $n_{crit} = \delta^2/4g^2 \simeq 40$. In this limit, the system Hamiltonian $\mathcal{H}_{tot} = \mathcal{H}_r + \mathcal{H}_q + \mathcal{H}_g + \mathcal{H}_d$ comprises the bare resonator Hamiltonian $\mathcal{H}_r = \hbar\omega_r n_r$, the qubit Hamiltonian $\mathcal{H}_q = \hbar\omega_q\hat{\sigma}_z/2$, the coupling Hamiltonian $\mathcal{H}_g = \hbar\chi\,[n_r + 1/2]\,\hat{\sigma}_z$, and a driving term $\mathcal{H}_d = \hbar\Omega_d\cos(\omega_d t)\hat{\sigma}_x$. Here, $\hat{\sigma}_i$ are the Pauli operators and Ω_d defines the amplitude of the excitation drive with frequency ω_d. We use the qubit state dependent ac-Stark shift defined by $\mathcal{H}_g$ for readout [52]. In Fig. 9 (b), we show driven Rabi oscillations continuously recorded during a weak measurement using $n_{RO} \simeq 0.1$ readout photons.

Appendix B: Coupling of thermal fields into a resonator

In this section, we derive how thermally induced voltage fluctuations on the feedlines influence the resonator population. Since we generate the thermal states out-

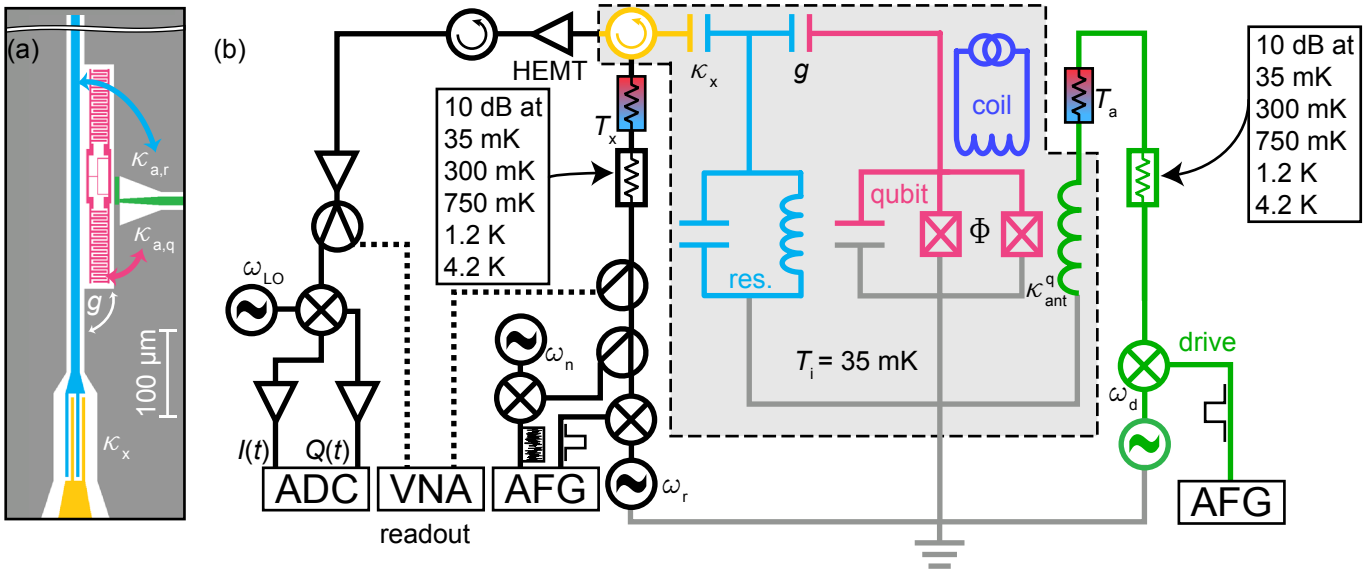

Figure 8. (a) Sample design: The frequency-tunable transmon qubit is capacitively coupled with coupling strength g to a readout resonator, which itself is coupled with rate κ_{x} to a readout line. Furthermore, the qubit is coupled with rate $\kappa_{\mathrm{a,q}}$ to a 50 Ω-matched on-chip antenna and with rate $\kappa_{\mathrm{a,r}}$ to the resonator. (b) Schematic drawing of the experimental setup. We can inject thermal states into antenna and resonator by controlling the temperature T_{x} and T_{a} of heatable attenuators while stabilizing the sample stage (enclosed by the dashed box) at $T_{\mathrm{i}} = 35\,\mathrm{mK}$.

side the resonator, the mean photon population n_{r} inside the resonator can be calculated as a cavity field which is coupled to several bosonic baths each described by a

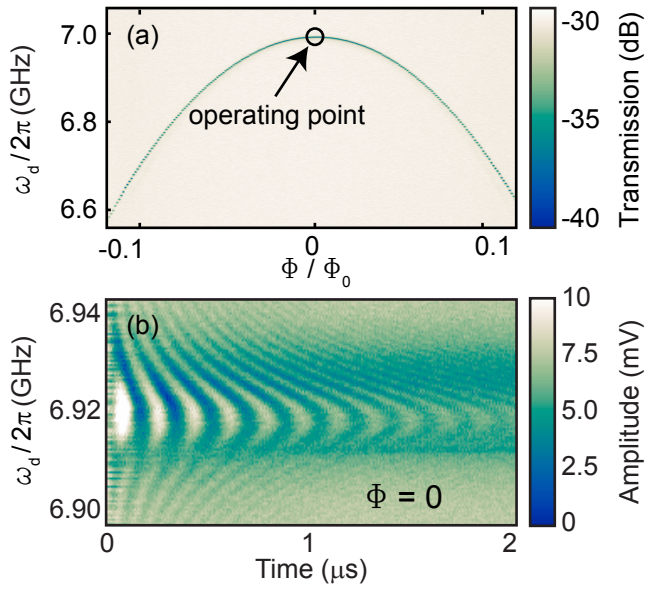

Figure 9. (a) Color encoded transmission magnitude plotted versus magnetic flux and drive frequency ω_{d} measured in a continuous wave two-tone experiment. All measurements are performed at the flux sweet spot of the transmon qubit. (b) Driven Rabi oscillations encoded in the frequency dependent transmission amplitude plotted versus evolution time and drive frequency ω_{d}.

Hamiltonian $\mathcal{H}_{\mathrm{bath}} = \sum_k \hbar\omega_k \hat{b}^\dagger_{k,j}\hat{b}_{k,j}$. Here, the respective field operators $\hat{b}^\dagger_k$, $(\hat{b}_k)$ create (annihilate) the individual field modes with frequencies ω_k. In our setup the three bosonic reservoirs ($j = $ i,x,a) couple to the resonator modes described by the operators $\hat{a}$, $\hat{a}^\dagger$ via the interaction Hamiltonian $\mathcal{H}_{\mathrm{int}} = -\imath\hbar\sum_k[\kappa_{k,j}\hat{a}^\dagger\hat{b}_{k,j} - \kappa_{k,j}\hat{b}^\dagger_{k,j}\hat{a}]$. For convenience, we split up the transmission line modes into a classical part $\bar{b}_k$ originating from a coherent drive, and into a quantum part $\hat{\xi}_k$, such that $\hat{b}_k(t) = e^{-\imath\omega_k t}\bar{b}_k + \hat{\xi}_k(t)$ [66]. The quantum part describes voltage fluctuations emitted from the heatable attenuators and will be the focus of the following discussion. The attenuators emit a voltage $V(t) = V_{\mathrm{vac}}[\hat{\xi}_k(t) + \hat{\xi}^\dagger_k(t)]$, which is fluctuating in time and has a Gaussian amplitude distribution. Here, V_{vac} is the vacuum amplitude of the corresponding mode. For a finite temperature, the correlation function for the voltage fluctuations is defined by the Hurwitz function [67–69]. The power spectral density of thermal fields $\mathcal{S}(\omega)$ in Eq. (1) can then be obtained by a Fourier transform [49, 50] of the correlation function. We now discuss how thermal fields described by $\mathcal{S}(\omega)$ enter the resonator. It can be shown, that the power spectrum inside the resonator is the product of the resonator modes and the modes entering from outside [70]. Consequently, the relation between the field operator $\hat{a}$ inside the resonator and the input field reads [71]

$$\hat{a}(\omega_{\mathrm{r}}) = \sum_{j=\mathrm{i,x,ant}} \sum_k \frac{\sqrt{\kappa_{k,j}}\hat{b}_{k,j}(\omega_k)}{\kappa_{\mathrm{tot}}/2 - \imath[\omega_k - \omega_{\mathrm{r}}]}\,. \qquad \text{(B1)}$$

Due to the high density of modes, we take the continuum limit $(\sum_k \mapsto \int \mathrm{d}\omega_k)$ and obtain the expression

$n_\mathrm{r}(\omega,T)\approx\mathcal{F}_\mathrm{L}(\omega)\sum_j\kappa_j n_j(\omega,T)$ presented in the main text. For a large qubit-resonator detuning $\delta\gg g,\kappa_\mathrm{tot}$, we can neglect the influence of qubit excitations entering the resonator. In this case, the Markovian master equation

$$\begin{aligned}\frac{\partial\hat{\rho}_\mathrm{r}}{\partial t}=&-\imath[\omega_\mathrm{r}\hat{a}^\dagger\hat{a},\hat{\rho}_\mathrm{r}]+\{n_\mathrm{i}\kappa_\mathrm{i}+n_\mathrm{x}\kappa_\mathrm{x}+n_\mathrm{a}\kappa_\mathrm{a,r}\}\,\mathcal{D}(\hat{a}^\dagger)\hat{\rho}_\mathrm{r}\\&+\{(n_\mathrm{i}+1)\kappa_\mathrm{i}+(n_\mathrm{x}+1)\kappa_\mathrm{x}+(n_\mathrm{a}+1)\kappa_\mathrm{a,r}\}\,\mathcal{D}(\hat{a})\hat{\rho}_\mathrm{r}\,,\end{aligned}\tag{B2}$$

describes the resonator, where $\hat{\rho}_\mathrm{r}$ is the density matrix of the undisturbed resonator and $\mathcal{D}(\hat{L})$ is the Lindblad operator. In the steady state limit, Eq. (B2) becomes

$$n_\mathrm{r}=\frac{n_\mathrm{i}\kappa_\mathrm{i}+n_\mathrm{x}\kappa_\mathrm{x}+n_\mathrm{a}\kappa_\mathrm{a,r}}{\kappa_\mathrm{i}+\kappa_\mathrm{x}+\kappa_\mathrm{a,r}}\,.\tag{B3}$$

This equation shows that we can precisely control the power inside the resonator using thermal photons emitted from the heatable attenuators. Concerning power, the nature of the photons inside the resonator (e.g., thermal or coherent) makes no difference.

Appendix C: First- and second-order coupling between thermal fields and the qubit

In this section, we derive the first-order and second-order dephasing rates for the transmon qubit due to thermal fields on on-chip control lines.

First-order coupling First-order coupling between flux fluctuations $\delta\lambda\equiv\delta\Phi/\Phi_0$ and the qubit follow the Hamiltonian $\mathcal{H}_\mathrm{sys}=[\hbar/2][\omega_\mathrm{q}\hat{\sigma}_\mathrm{z}+\delta\omega_\mathrm{q}\hat{\sigma}_\mathrm{z}]$. Here, $\delta\omega_\mathrm{q}=\delta\lambda\mathcal{D}^{(1)}_{\lambda,\mathrm{z}}$ describes fluctuations of the qubit transition frequency leading to dephasing characterized by the first-order transfer function

$$\mathcal{D}^{(1)}_{\lambda,\mathrm{z}}(\lambda^\star)\equiv\frac{1}{\hbar}\,\frac{\partial\mathcal{H}_\mathrm{q}(\lambda)}{\partial\lambda}\bigg|_{\lambda^\star}=-\,\frac{\pi\omega_{\mathrm{q},0}}{2}\,\frac{\sin(\pi\lambda)}{\sqrt{\cos(\pi\lambda)}}\bigg|_{\lambda^\star}\,.\tag{C1}$$

Equation (C1) is defined at flux operating points $\lambda^\star\in[-1/2,\,1/2]$ using the transmon qubit Hamiltonian $\mathcal{H}_\mathrm{q}=\hbar\omega_{\mathrm{q},0}\sqrt{|\cos(\pi\lambda)|}$. To analyze the fluctuations $\delta\omega_\mathrm{q}$, we first derive how voltage fluctuations δV on the antenna line are converted into flux fluctuations $\delta\lambda$ in the SQUID loop. Because the antenna is short-circuited near the qubit by a finite inductance L_a as depicted in Fig. 10, we describe it as a first-order low-pass LR filter, i.e., $Z_\mathrm{a}(\omega)\approx\omega^2L_\mathrm{a}^2/Z_0$ (similar to the way presented in Ref. 72). The finite inductance L_a of the short-circuit converts voltage fluctuations δV emitted from the attenuator into current fluctuations $\delta I=\delta V(\imath\omega L_\mathrm{a})^{-1}$. Via the mutual inductance M_a between antenna and SQUID loop, these current fluctuations cause flux fluctuations $\delta\lambda=M_\mathrm{a}\delta I/\Phi_0$. Using the transfer function in Eq. (C1), we calculate the resulting change in transition frequency to

$$\begin{aligned}\delta\omega_\mathrm{q}(\lambda^\star)&=\mathcal{D}^{(1)}_{\lambda,\mathrm{z}}(\lambda^\star)\times\delta\lambda\\&=\mathcal{D}^{(1)}_{\lambda,\mathrm{z}}(\lambda^\star)\frac{M_\mathrm{a}}{\Phi_0}\frac{\delta V}{\imath\omega L_\mathrm{a}}\,.\end{aligned}\tag{C2}$$

This equation shows that thermally induced voltage fluctuations indeed lead to fluctuations $\delta\omega_\mathrm{q}$ of the qubit transition frequency. To calculate the resulting dephasing rate we use the spectral function

$$\begin{aligned}\langle\delta\omega_\mathrm{q}(t)\delta\omega_\mathrm{q}(0)\rangle_\omega&=\left[\frac{\mathcal{D}^{(1)}_{\lambda,\mathrm{z}}(\lambda^\star)M_\mathrm{a}}{\omega L_\mathrm{a}\Phi_0}\right]^2\langle\delta V(t)\delta V(0)\rangle_\omega\\&=\left[\frac{\mathcal{D}^{(1)}_{\lambda,\mathrm{z}}(\lambda^\star)M_\mathrm{a}}{\omega L_\mathrm{a}\Phi_0}\right]^2\mathrm{Re}\{Z_\mathrm{a}(\omega)\}\mathcal{S}(\omega)\\&=\left[\mathcal{D}^{(1)}_{\lambda,\mathrm{z}}(\lambda^\star)\frac{M_\mathrm{a}}{\Phi_0}\right]^2\frac{\mathcal{S}(\omega)}{Z_0}\end{aligned}\tag{C3}$$

of these fluctuations. Here, we use the fluctuation dissipation theorem $\langle\delta V(t)\delta V(0)\rangle_\omega=\mathrm{Re}\{Z_\mathrm{a}(\omega)\}\mathcal{S}(\omega)$ [73, 74] to relate the voltage fluctuations to their power spectral density. The expression $\langle\delta V(t)\delta V(0)\rangle_\omega$ displays the spectral weight of the fluctuations with units V^2/Hz. The fluctuations of the qubit transition frequency defined in Eq. (C3) lead to random fluctuations $\delta\phi(t)=\int_0^t\mathrm{d}t'\delta\omega_\mathrm{q}(t')$ of the qubit phase relative to its mean phase $\bar{\phi}$ in a rotating frame. Assuming thermal states to be Gaussian [31, 33] and $1/f$ contributions to be negligible, the phase fluctuations in turn lead to a single exponential decay function [65]

$$\begin{aligned}\langle\hat{\sigma}_-(t)\hat{\sigma}_+(0)\rangle&\approx\exp\left[-\gamma_2t-\langle\delta\phi^2\rangle/2\right]\\&=\exp\left[-\gamma_2t-\frac{1}{2}\int\int_0^t\mathrm{d}t_1\mathrm{d}t_2\langle\delta\omega_\mathrm{q}(t_1)\delta\omega_\mathrm{q}(t_2)\rangle\right]\\&=\exp\left[-\gamma_2t-\frac{1}{2}\left[\mathcal{D}^{(1)}_{\lambda,\mathrm{z}}(\lambda^\star)\frac{M_\mathrm{a}}{\Phi_0}\right]^2\frac{\mathcal{S}(\omega)}{Z_0}t\right]\,.\end{aligned}\tag{C4}$$

Here, we make use of the fact that the correlation function $\langle\delta\omega_\mathrm{q}(t_1)\delta\omega_\mathrm{q}(t_2)\rangle$ is a δ-function at low frequencies. The additional decoherence due to thermal states on the antenna line is therefore given as

$$\gamma^{(1)}_{\varphi,\mathrm{a}}=\left[\mathcal{D}^{(1)}_{\lambda,\mathrm{z}}(\lambda^\star)\frac{M_\mathrm{a}}{\Phi_0}\right]^2\frac{\mathcal{S}(\omega)}{2Z_0}\approx\left[\mathcal{D}^{(1)}_{\lambda,\mathrm{z}}(\lambda^\star)\frac{M_\mathrm{a}}{\Phi_0}\right]^2\frac{k_\mathrm{B}T_\mathrm{a}}{Z_0}\,.\tag{C5}$$

The approximation on the right-hand side of Eq. (C5) reflects the low-frequency limit by setting $\mathcal{S}(\omega\mapsto0)=k_\mathrm{B}T_\mathrm{a}$, which shows that dephasing due to propagating thermal fields is expected to increase linearly with the temperature T_a of the black-body radiator.

The above derivation of the qubit dephasing rate is equivalent to the result derived from the spin-boson model, where the dephasing is defined as [72]

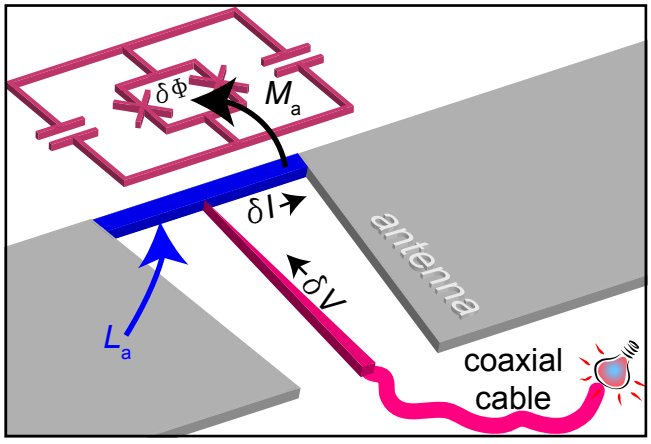

Figure 10. Sketch of the short-circuited antenna line, which converts voltage fluctuations δV into flux fluctuations $\delta\Phi$ inside the SQUID loop of the transmon. The region forming the short-circuit has an inductance L_a and a mutual inductance M_a to the SQUID loop. The propagating thermal fields are guided through a coaxial cable to the sample and are thus only located on the antenna structure.

$\gamma^{(1)}_{\varphi,\mathrm{a}} = 2\pi\alpha\mathcal{S}(\omega\mapsto 0)/\hbar$. Here, the dimensionless dissipation parameter α is defined as [31]

$$\alpha \equiv \frac{R_\mathrm{q}}{Z_0}\left[\hbar\mathcal{D}^{(1)}_{\lambda,\mathrm{z}}(\lambda^\star)\frac{\partial\lambda}{\partial\Phi}\frac{M_\mathrm{a}}{\Phi_0}\right]^2 = \frac{\hbar}{2\pi Z_0}\left[\mathcal{D}^{(1)}_{\lambda,\mathrm{z}}(\lambda^\star)\frac{M_\mathrm{a}}{\Phi_0}\right]^2 \tag{C6}$$

and $R_\mathrm{q} \equiv h/4e^2$ is the quantum resistance for Cooper pairs. We note that the spin-boson model can be applied to calculate the dephasing rate because the antenna creates an ohmic environment if modeled as an LR-filter and because thermal noise has no $1/f$ contribution.

Second-order coupling When the transmon qubit is operated at the flux sweet spot, dephasing can be dominated from intensity fluctuations coupling in second-order to the qubit. These second-order fluctuations

$$\delta\lambda^2 \equiv \frac{\delta\Phi^2}{\Phi_0^2} = \frac{M_\mathrm{a}^{(2)}\delta I^2}{\hbar\omega_{\mathrm{q},0}} = \frac{M_\mathrm{a}^2}{L_\ell}\frac{\delta I^2}{\hbar\omega_{\mathrm{q},0}} \tag{C7}$$

are normalized to the relevant energy scale $\hbar\omega_{\mathrm{q},0}$ of the qubit and scale with the second-order mutual inductance $M_\mathrm{a}^{(2)} = M_\mathrm{a}^2/L_\ell$ due to the inductive energy $E_\ell = \Phi_0^2/2L_\ell$ of the SQUID loop with inductance L_ℓ. The intensity fluctuations induce fluctuations $\delta\omega_\mathrm{q} = \mathcal{D}^{(2)}_{\lambda,\mathrm{z}}\delta\lambda^2/2$ of the qubit transition frequency leading to dephasing based on the system Hamiltonian $\mathcal{H}_\mathrm{sys}$ defined in the previous paragraph. The frequency fluctuations are characterized by the second-order derivative of the qubit transition frequency

$$\begin{aligned}\mathcal{D}^{(2)}_{\lambda,\mathrm{z}}(\lambda^\star) &\equiv \frac{1}{\hbar}\left.\frac{\partial^2\mathcal{H}_\mathrm{q}(\lambda)}{\partial\lambda^2}\right|_{\lambda^\star} \\ &= -\frac{\pi^2\omega_{\mathrm{q},0}}{2}\sqrt{\cos(\pi\lambda)} - \left.\frac{\pi^2\omega_{\mathrm{q},0}}{4}\frac{\sin^2(\pi\lambda)}{\cos^{3/2}(\pi\lambda)}\right|_{\lambda^\star}.\end{aligned} \tag{C8}$$

Using this transfer function as well as $\delta V^2 = (\omega L_\mathrm{a})^2\delta I^2$, we can characterize fluctuations in the qubit transition frequency similar to Eq. (C3) as

$$\begin{aligned}\langle\delta\omega_\mathrm{q}(t)\delta\omega_\mathrm{q}(0)\rangle_\omega &= \left[\frac{\mathcal{D}^{(2)}_{\lambda,\mathrm{z}}(\lambda^\star)}{2}\right]^2\langle\delta\lambda^2(t)\delta\lambda^2(0)\rangle_\omega \\ &= \left[\frac{\mathcal{D}^{(2)}_{\lambda,\mathrm{z}}(\lambda^\star)}{2}\frac{M_\mathrm{a}^2}{L_\ell}\frac{1}{\omega^2L_\mathrm{a}^2}\right]^2\frac{\langle\delta V^2(t)\delta V^2(0)\rangle_\omega}{(\hbar\omega_{\mathrm{q},0})^2} \\ &= \left[\frac{\mathcal{D}^{(2)}_{\lambda,\mathrm{z}}(\lambda^\star)}{2}\frac{M_\mathrm{a}^2}{L_\ell}\frac{1}{\omega^2L_\mathrm{a}^2}\right]^2\mathrm{Re}\{Z_\mathrm{a}(\omega)\}^2\frac{\mathcal{S}^{(2)}(\omega)}{(\hbar\omega_{\mathrm{q},0})^2} \\ &= \left[\frac{\mathcal{D}^{(2)}_{\lambda,\mathrm{z}}(\lambda^\star)}{2}\frac{M_\mathrm{a}^2}{L_\ell}\right]^2\frac{\mathcal{S}^{(2)}(\omega)}{(\hbar\omega_{\mathrm{q},0})^2Z_0^2}.\end{aligned} \tag{C9}$$

where $\mathcal{S}^{(2)}(\omega)$ is the second-order spectral density defined in Eq. (2). To derive the dephasing rate using Eq. (C9), we have to consider the statistical properties of $\mathcal{S}^{(2)}(\omega)$. Because the intensity fluctuations are not Gaussian distributed [31], applying an approach similar to the one in Eq. (C4) to calculate the dephasing rate from second-order thermal fields is not valid in general. Performing only first-order pertubative analysis, we can, however, assume that the second-order fluctuations are Gaussian distributed with a width that is defined by $\mathcal{S}^{(2)}(\omega)$. Then, we find the additional dephasing rate due to second-order noise

$$\begin{aligned}\gamma^{(2)}_{\varphi,\mathrm{a}} &= \left[\frac{\mathcal{D}^{(2)}_{\lambda,\mathrm{z}}(\lambda^\star)}{2}\frac{M_\mathrm{a}^2}{L_\ell}\right]^2\frac{\mathcal{S}^{(2)}(\omega)}{(\hbar\omega_{\mathrm{q},0})^2Z_0^2} \\ &\approx \underbrace{\left[\frac{\mathcal{D}^{(2)}_{\lambda,\mathrm{z}}(\lambda^\star)}{2\sqrt{3}}\frac{M_\mathrm{a}^2}{L_\ell Z_0}\right]^2}_{\alpha^{(2)}}\underbrace{\left[\frac{k_\mathrm{B}T_\mathrm{a}}{\hbar\omega_{\mathrm{q},0}}\right]^2}_{r}\frac{2\pi k_\mathrm{B}T_\mathrm{a}}{\hbar},\end{aligned} \tag{C10}$$

taking the low-frequency limit $\mathcal{S}^{(2)}(\omega\mapsto 0) \approx 2\pi k_\mathrm{B}^3T_\mathrm{a}^3/3\hbar$ obtained from Eq. (2). Just as the first-order dephasing rate, the second-order dephasing rate is equivalent to an approach based on the spin-boson model when using the second-order dissipation factor $\alpha^{(2)}$. When comparing Eq. (C10) to Eq. (C5), we see that second-order thermal noise is suppressed by the factor r if the thermal energy is lower than the qubit energy. Hence, we have to use temperatures $T_\mathrm{a} > \hbar\omega_{\mathrm{q},0}/k_\mathrm{B}$ or work at the flux sweet spot to observe the T^3 law.

[1] E. Lucero, R. Barends, Y. Chen, J. Kelly, M. Mariantoni, A. Megrant, P. O'Malley, D. Sank, A. Vainsencher, J. Wenner, T. White, Y. Yin, A. N. Cleland, and J. M. Martinis, Nat. Phys. **8**, 719 (2012).

[2] A. A. Houck, H. E. Türeci, and J. Koch, Nat. Phys. **8**, 292 (2012).

[3] K. G. Fedorov, L. Zhong, S. Pogorzalek, P. Eder, M. Fischer, J. Goetz, E. Xie, F. Wulschner, K. Inomata, T. Yamamoto, Y. Nakamura, R. Di Candia, U. Las Heras, M. Sanz, E. Solano, E. P. Menzel, F. Deppe, A. Marx, and R. Gross, Phys. Rev. Lett. **117**, 020502 (2016).

[4] A. Wallraff, D. I. Schuster, A. Blais, L. Frunzio, R.-S. Huang, J. Majer, S. Kumar, S. M. Girvin, and R. J. Schoelkopf, Nature **431**, 162 (2004).

[5] C. W. Zollitsch, K. Mueller, D. P. Franke, S. T. B. Goennenwein, M. S. Brandt, R. Gross, and H. Huebl, Appl. Phys. Lett. **107**, 142105 (2015).

[6] T. Niemczyk, F. Deppe, H. Hübl, E. P. Menzel, F. Hocke, M. J. Schwarz, J. J. Garcia-Ripoll, D. Zueco, T. Hümmer, E. Solano, A. Marx, and R. Gross, Nat. Phys. **6**, 772 (2010).

[7] P. Forn-Díaz, J. Lisenfeld, D. Marcos, J. J. Garcia-Ripoll, E. Solano, C. J. P. M. Harmans, and J. E. Mooij, Phys. Rev. Lett. **105**, 237001 (2010).

[8] A. Baust, E. Hoffmann, M. Haeberlein, M. J. Schwarz, P. Eder, J. Goetz, F. Wulschner, E. Xie, L. Zhong, F. Quijandría, D. Zueco, J.-J. G. Ripoll, L. García-Álvarez, G. Romero, E. Solano, K. G. Fedorov, E. P. Menzel, F. Deppe, A. Marx, and R. Gross, Phys. Rev. B **93**, 214501 (2016).

[9] T. Hime, P. A. Reichardt, B. L. T. Plourde, T. L. Robertson, C.-E. Wu, A. V. Ustinov, and J. Clarke, Science **314**, 1427 (2006).

[10] A. O. Niskanen, K. Harrabi, F. Yoshihara, Y. Nakamura, S. Lloyd, and J. S. Tsai, Science **316**, 723 (2007).

[11] R. C. Bialczak, M. Ansmann, M. Hofheinz, M. Lenander, E. Lucero, M. Neeley, A. D. O'Connell, D. Sank, H. Wang, M. Weides, J. Wenner, T. Yamamoto, A. N. Cleland, and J. M. Martinis, Phys. Rev. Lett. **106**, 060501 (2011).

[12] A. Baust, E. Hoffmann, M. Haeberlein, M. J. Schwarz, P. Eder, J. Goetz, F. Wulschner, E. Xie, L. Zhong, F. Quijandría, B. Peropadre, D. Zueco, J.-J. García Ripoll, E. Solano, K. Fedorov, E. P. Menzel, F. Deppe, A. Marx, and R. Gross, Phys. Rev. B **91**, 014515 (2015).

[13] Wulschner, F., Goetz, J., Koessel, F. R., Hoffmann, E., Baust, A., Eder, P., Fischer, M., Haeberlein, M., Schwarz, M. J., Pernpeintner, M., Xie, E., Zhong, L., Zollitsch, C. W., Peropadre, B., Garcia Ripoll, J.-J., Solano, E., Fedorov, K. G., Menzel, E. P., Deppe, F., Marx, A., and Gross, R., EPJ Quant. Tech. **3**, 10 (2016).

[14] R. W. Simmonds, K. M. Lang, D. A. Hite, S. Nam, D. P. Pappas, and J. M. Martinis, Phys. Rev. Lett. **93**, 077003 (2004).

[15] Y. Shalibo, Y. Rofe, D. Shwa, F. Zeides, M. Neeley, J. M. Martinis, and N. Katz, Phys. Rev. Lett. **105**, 177001 (2010).

[16] J. Lisenfeld, C. Müller, J. H. Cole, P. Bushev, A. Lukashenko, A. Shnirman, and A. V. Ustinov, Phys. Rev. Lett. **105**, 230504 (2010).

[17] M. D. Reed, B. R. Johnson, A. A. Houck, L. DiCarlo, J. M. Chow, D. I. Schuster, L. Frunzio, and R. J. Schoelkopf, Appl. Phys. Lett. **96**, 203110 (2010).

[18] Z. Kim, B. Suri, V. Zaretskey, S. Novikov, K. D. Osborn, A. Mizel, F. C. Wellstood, and B. S. Palmer, Phys. Rev. Lett. **106**, 120501 (2011).

[19] V. Zaretskey, S. Novikov, B. Suri, Z. Kim, F. C. Wellstood, and B. S. Palmer, J. Appl. Phys. **114**, 094305 (2013).

[20] N. T. Bronn, Y. Liu, J. B. Hertzberg, A. D. Corcoles, A. A. Houck, J. M. Gambetta, and J. M. Chow, Appl. Phys. Lett. **107**, 172601 (2015).

[21] M. Haeberlein, F. Deppe, A. Kurcz, J. Goetz, A. Baust, P. Eder, K. Fedorov, M. Fischer, E. P. Menzel, M. J. Schwarz, F. Wulschner, E. Xie, L. Zhong, E. Solano, and J.-J. R. G. Marx, Achim García-Ripoll, ArXiv e-prints (2015), arXiv:1506.09114 [cond-mat].

[22] O. Astafiev, Y. A. Pashkin, Y. Nakamura, T. Yamamoto, and J. S. Tsai, Phys. Rev. Lett. **96**, 137001 (2006).

[23] F. Yoshihara, K. Harrabi, A. O. Niskanen, Y. Nakamura, and J. S. Tsai, Phys. Rev. Lett. **97**, 167001 (2006).

[24] R. H. Koch, D. P. DiVincenzo, and J. Clarke, Phys. Rev. Lett. **98**, 267003 (2007).

[25] J. A. Schreier, A. A. Houck, J. Koch, D. I. Schuster, B. R. Johnson, J. M. Chow, J. M. Gambetta, J. Majer, L. Frunzio, M. H. Devoret, S. M. Girvin, and R. J. Schoelkopf, Phys. Rev. B **77**, 180502 (2008).

[26] G. Burkard, Phys. Rev. B **79**, 125317 (2009).

[27] J. Bylander, S. Gustavsson, F. Yan, F. Yoshihara, K. Harrabi, G. Fitch, D. G. Cory, Y. Nakamura, J.-S. Tsai, and W. D. Oliver, Nat. Phys. **7**, 565 (2011).

[28] A. A. Houck, J. A. Schreier, B. R. Johnson, J. M. Chow, J. Koch, J. M. Gambetta, D. I. Schuster, L. Frunzio, M. H. Devoret, S. M. Girvin, and R. J. Schoelkopf, Phys. Rev. Lett. **101**, 080502 (2008).

[29] D. Vion, A. Aassime, A. Cottet, P. Joyez, H. Pothier, C. Urbina, D. Esteve, and M. H. Devoret, Science **296**, 886 (2002).

[30] J. Koch, T. M. Yu, J. Gambetta, A. A. Houck, D. I. Schuster, J. Majer, A. Blais, M. H. Devoret, S. M. Girvin, and R. J. Schoelkopf, Phys. Rev. A **76**, 042319 (2007).

[31] A. Shnirman, Y. Makhlin, and G. Schön, Phys. Scripta **2002**, 147 (2002).

[32] Y. Makhlin and A. Shnirman, J. Exp. and Theor. Phys. Lett. **78**, 0021 (2003).

[33] Y. Makhlin and A. Shnirman, Phys. Rev. Lett. **92**, 178301 (2004).

[34] H. Paik, D. I. Schuster, L. S. Bishop, G. Kirchmair, G. Catelani, A. P. Sears, B. R. Johnson, M. J. Reagor, L. Frunzio, L. I. Glazman, S. M. Girvin, M. H. Devoret, and R. J. Schoelkopf, Phys. Rev. Lett. **107**, 240501 (2011).

[35] F. Yan, J. Bylander, S. Gustavsson, F. Yoshihara, K. Harrabi, D. G. Cory, T. P. Orlando, Y. Nakamura, J.-S. Tsai, and W. D. Oliver, Phys. Rev. B **85**, 174521 (2012).

[36] C. Müller, J. Lisenfeld, A. Shnirman, and S. Poletto, Phys. Rev. B **92**, 035442 (2015).

[37] F. Yan, S. Gustavsson, A. Kamal, J. Birenbaum, A. P. Sears, D. Hover, D. Rosenberg, G. Samach, T. J. Gudmundsen, J. L. Yoder, T. P. Orlando, J. Clarke, A. J.

Kerman, and W. D. Oliver, ArXiv e-prints (2015), arXiv:1508.06299.
[38] M. Mariantoni, E. P. Menzel, F. Deppe, M. A. Araque Caballero, A. Baust, T. Niemczyk, E. Hoffmann, E. Solano, A. Marx, and R. Gross, Phys. Rev. Lett. **105**, 133601 (2010).
[39] E. P. Menzel, F. Deppe, M. Mariantoni, M. A. Araque Caballero, A. Baust, T. Niemczyk, E. Hoffmann, A. Marx, E. Solano, and R. Gross, Phys. Rev. Lett. **105**, 100401 (2010).
[40] E. P. Menzel, R. Di Candia, F. Deppe, P. Eder, L. Zhong, M. Ihmig, M. Haeberlein, A. Baust, E. Hoffmann, D. Ballester, K. Inomata, T. Yamamoto, Y. Nakamura, E. Solano, A. Marx, and R. Gross, Phys. Rev. Lett. **109**, 250502 (2012).
[41] P. Bertet, I. Chiorescu, G. Burkard, K. Semba, C. J. P. M. Harmans, D. P. DiVincenzo, and J. E. Mooij, Phys. Rev. Lett. **95**, 257002 (2005).
[42] A. D. Corcoles, J. M. Chow, J. M. Gambetta, C. Rigetti, J. R. Rozen, G. A. Keefe, M. Beth Rothwell, M. B. Ketchen, and M. Steffen, Appl. Phys. Lett. **99**, 181906 (2011).
[43] J. M. Sage, V. Bolkhovsky, W. D. Oliver, B. Turek, and P. B. Welander, J. Appl. Phys. **109**, 063915 (2011).
[44] A. P. Sears, A. Petrenko, G. Catelani, L. Sun, H. Paik, G. Kirchmair, L. Frunzio, L. I. Glazman, S. M. Girvin, and R. J. Schoelkopf, Phys. Rev. B **86**, 180504 (2012).
[45] C. Rigetti, J. M. Gambetta, S. Poletto, B. L. T. Plourde, J. M. Chow, A. D. Córcoles, J. A. Smolin, S. T. Merkel, J. R. Rozen, G. A. Keefe, M. B. Rothwell, M. B. Ketchen, and M. Steffen, Phys. Rev. B **86**, 100506 (2012).
[46] I. M. Pop, K. Geerlings, G. Catelani, R. J. Schoelkopf, L. I. Glazman, and M. H. Devoret, Nature **508**, 369 (2014).
[47] J. Goetz, F. Deppe, M. Haeberlein, F. Wulschner, C. W. Zollitsch, S. Meier, M. Fischer, P. Eder, E. Xie, K. G. Fedorov, E. P. Menzel, A. Marx, and R. Gross, J. App. Phys. **119**, 015304 (2016).
[48] Bose, Z. Phys. **26**, 178 (1924).
[49] R. J. Schoelkopf, P. J. Burke, A. A. Kozhevnikov, D. E. Prober, and M. J. Rooks, Phys. Rev. Lett. **78**, 3370 (1997).
[50] J. M. Martinis, S. Nam, J. Aumentado, K. M. Lang, and C. Urbina, Phys. Rev. B **67**, 094510 (2003).
[51] D. M. Pozar, *Microwave engineering*, 4th ed. (Wiley, 2012).
[52] D. I. Schuster, A. Wallraff, A. Blais, L. Frunzio, R.-S. Huang, J. Majer, S. M. Girvin, and R. J. Schoelkopf, Phys. Rev. Lett. **94**, 123602 (2005).
[53] O. Astafiev, Y. A. Pashkin, Y. Nakamura, T. Yamamoto, and J. S. Tsai, Phys. Rev. Lett. **93**, 267007 (2004).
[54] G. Catelani, J. Koch, L. Frunzio, R. J. Schoelkopf, M. H. Devoret, and L. I. Glazman, Phys. Rev. Lett. **106**, 077002 (2011).
[55] M. Lenander, H. Wang, R. C. Bialczak, E. Lucero, M. Mariantoni, M. Neeley, A. D. O'Connell, D. Sank, M. Weides, J. Wenner, T. Yamamoto, Y. Yin, J. Zhao, A. N. Cleland, and J. M. Martinis, Phys. Rev. B **84**, 024501 (2011).
[56] E. M. Purcell, H. C. Torrey, and R. V. Pound, Phys. Rev. **69**, 37 (1946).
[57] E. A. Sete, J. M. Gambetta, and A. N. Korotkov, Phys. Rev. B **89**, 104516 (2014).
[58] A. Blais, R.-S. Huang, A. Wallraff, S. M. Girvin, and R. J. Schoelkopf, Phys. Rev. A **69**, 062320 (2004).
[59] M. Boissonneault, J. M. Gambetta, and A. Blais, Phys. Rev. A **79**, 013819 (2009).
[60] J. Goetz, S. Pogorzalek, F. Deppe, K. G. Fedorov, P. Eder, M. Fischer, F. Wulschner, E. Xie, A. Marx, and R. Gross, ArXiv e-prints (2016), arXiv:1609.07353 [quant-ph].
[61] C. Schuster and W. Fichtner, IEEE T. Electromagn. C. **43**, 416 (2001).
[62] J. Burnett, L. Faoro, I. Wisby, V. L. Gurtovoi, A. V. Chernykh, G. M. Mikhailov, V. A. Tulin, R. Shaikhaidarov, V. Antonov, P. J. Meeson, A. Y. Tzalenchuk, and T. Lindström, Nat. Commun. **5**, (2014).
[63] L. Faoro and L. B. Ioffe, Phys. Rev. B **91**, 014201 (2015).
[64] J. Lisenfeld, G. J. Grabovskij, C. Müller, J. H. Cole, G. Weiss, and A. V. Ustinov, Nat. Commun. **6**, (2015).
[65] J. Gambetta, A. Blais, D. I. Schuster, A. Wallraff, L. Frunzio, J. Majer, M. H. Devoret, S. M. Girvin, and R. J. Schoelkopf, Phys. Rev. A **74**, 042318 (2006).
[66] M. Devoret, B. Huard, R. Schoelkopf, and L. Cugliandolo, *Quantum Machines: Measurement and Control of Engineered Quantum Systems: Lecture Notes of the Les Houches Summer School: Volume 96, July 2011*, Lecture Notes of the Les Houches Summer School (OUP Oxford, 2014) p. 231.
[67] Y. Kano and E. Wolf, P. Phys. Soc. **80**, 1273 (1962).
[68] C. Mehta, Il Nuovo Cimento **28**, 401 (1963).
[69] L. J. Klein, H. F. Hamann, Y.-Y. Au, and S. Ingvarsson, Appl. Phys. Lett. **92**, 213102 (2008).
[70] K. Ujihara, Phys. Rev. A **18**, 659 (1978).
[71] D. Walls and G. Milburn, *Quantum Optics* (Springer Berlin Heidelberg, 2008) p. 133.
[72] van der Wal, C. H., Wilhelm, F. K., Harmans, C. J.P.M., and Mooij, J. E., Eur. Phys. J. B **31**, 111 (2003).
[73] H. Nyquist, Phys. Rev. **32**, 110 (1928).
[74] H. B. Callen and T. A. Welton, Phys. Rev. **83**, 34 (1951).